Editors' Suggestion

Self-Organized Multifrequency Clusters in an Oscillating Electrochemical System with Strong Nonlinear Coupling

Maximilian Patzauer* and Katharina Krischer†

Nonequilibrium Chemical Physics, Department of Physics, Technical University of Munich, 85748 Garching, Germany

(Received 6 October 2020; revised 26 January 2021; accepted 9 April 2021; published 10 May 2021)

We study the spatiotemporal dynamics of the oscillatory photoelectrodissolution of *n*-type Si in a fluoride-containing electrolyte under anodic potentials using *in situ* ellipsometric imaging. When lowering the illumination intensity stepwise, we successively observe uniform oscillations, modulated amplitude clusters, and the coexistence of multifrequency clusters, i.e., regions with different frequencies, with a stationary domain. We argue that the multifrequency clusters emerge due to an adaptive, nonlinear, and nonlocal coupling, similar to those found in the context of neural dynamics.

DOI: 10.1103/PhysRevLett.126.194101

Much of the dynamics of oscillating systems as diverse as neural activities [1], electrical power grids [2], multimode lasers [3], and Josephson junction arrays [4] can be understood within the common framework of networks of coupled oscillators. These diverse applications render the study of coupled oscillators an important discipline of nonlinear dynamics. The overwhelming majority of previous studies consider the case of a linear coupling. Only recently, the more general case of nonlinear coupling has received increasing attention [5–14]. It could be shown that this generalization can produce genuine nonlinear coupling features. For example, the case of global nonlinear coupling has been found to produce self-organized quasiperiodicity in ensembles of phase oscillators [5], complex chimera states composed of (nearly) synchronized regions of different mean frequencies and incoherent regions [14], or a variety of coexistence patterns, including again chimera states [9–12]. Another representation of nonlinear coupling is realized in networks of Kuramoto oscillators that are designed to mimic adaptive neural networks [15]. In this type of model, recent studies predict the emergence of multifrequency clusters even when the oscillators are identical [16–18]. Until then, the existence of multifrequency clusters was always linked to heterogeneous oscillatory systems with some distribution of the natural frequencies [19–22].

In this Letter, we report the emergence of self-organized multifrequency clusters from a uniform oscillatory state during the photoelectrodissolution of an *n*-Si wafer when reducing the illumination intensity. Through the illumination, valence-band holes are created. Their movement parallel to the surface constitutes a nonlocal spatial coupling [23]. In addition, an external resistance in series with the electrode acts as a global synchronizing force on the dynamics [24]. Hence, there are two dominant types of coupling, a global synchronizing coupling and a long-range coupling through diffusion and migration of valence-band holes. Below we will argue that their interaction creates a nonlinear coupling that, in turn, promotes the formation of multifrequency clusters.

The oscillatory photoelectrodissolution of Si in fluoride-containing electrolytes involves the electrochemical oxidation of Si to SiO_2 according to

$$\mathrm{Si} + 2\mathrm{H_2O} + \lambda_{\mathrm{VB}} h^+ \rightarrow \mathrm{SiO_2} + 4\mathrm{H^+} + (4 - \lambda_{\mathrm{VB}}) e^-, \quad (1)$$

and the chemical etching of SiO_2 via

$$\mathrm{SiO_2} + 6\mathrm{HF} \rightarrow \mathrm{SiF_6^{2-}} + 2\mathrm{H_2O} + 2\mathrm{H^+}, \quad (2)$$

where $1 \leq \lambda_{\mathrm{VB}} \leq 4$ is the amount of valence-band holes h^+ [25].

We conducted our experiments with an *n*-doped (1–10 Ω cm) Si (111) sample as the working electrode in a three-electrode setup. The electrolyte was an aqueous solution containing 0.06 M NH_4F and 142 mM H_2SO_4. The uniformity of the electrode surface was monitored *in situ* with an ellipsometric imaging setup which probes the change in optical path length at the electrochemical interface. The changes in optical path length are converted into an intensity signal $\xi(\mathbf{x}, t)$ ($\mathbf{x}$ denoting space and t time) and recorded with a CCD camera (JAI CV-A50). We will present the ellipsometric intensity $\xi(\mathbf{x}, t)$ as a percentage of the saturation threshold of the CCD camera. To allow for the oxidation of *n*-type Si, the electrode was illuminated with a linearly polarized He-Ne laser (HNL150L-EC, Thorlabs), the intensity of which was adjusted with a

linear polarization filter. The illumination was uniform across the entire electrode surface. Further experimental details can be found in the Supplemental Material (SM) [26] and in [23].

In the measurement presented below, the illumination intensity is the bifurcation parameter. We initialized the electrode by applying a constant voltage at a high illumination intensity and then decreased the illumination step by step. At each step, we waited until transients had died out and then measured the dynamics for 10^3 s. We did not find any experimental evidence of hysteresis in the investigated parameter range. In order to characterize the dynamics of our system, we define the amplitude $A(\mathbf{x},t)$ and phase $\phi(\mathbf{x},t)$ of the ellipsometric intensity signal $\xi(\mathbf{x},t)$ at each pixel by calculating the analytic signal $\zeta(\mathbf{x},t)$ via the Hilbert transform $H[\xi(\mathbf{x},t)]$ (for details see [28]):

$$\zeta(\mathbf{x},t) = \xi(\mathbf{x},t) + iH[\xi(\mathbf{x},t)] = A(\mathbf{x},t)e^{i\phi(\mathbf{x},t)}. \quad (3)$$

Having determined the time series of the phase and of the amplitude, we extracted the dominant frequency $\nu(\mathbf{x})$ at each point from a linear fit to ϕ vs t (see SM [26]) and the temporally averaged amplitude $\overline{A(\mathbf{x},t)}$.

Exemplary states from a measurement series can be seen in Fig. 1 where the temporally averaged amplitude $\overline{A(\mathbf{x},t)}$, the dominant frequency $\nu(\mathbf{x})$, and a snapshot of the phase at an arbitrary instant in time, $\phi(\mathbf{x}, t = 807\ \text{s})$, are shown in the first, second, and third row, respectively. The four columns depict measurements at four different illumination intensities. The initial, highly illuminated state is shown in column I. Here, the system oscillates uniformly with the same amplitude, frequency, and phase at each point in space, cf. [9,29].

Upon lowering the illumination intensity (Fig. 1, column II), the electrode splits into a region with higher amplitude and a region with lower amplitude. These two regions oscillate with the same dominant frequency, but the oscillation phase differs between points in the higher- and lower-amplitude regions. In other words, amplitude clusters have formed. Note that the exact location of the clusters differs when the experiment is repeated, but the clusters tend to form along the edges of the electrode.

Yet, the data shown in Fig. 1, column II do not give the full picture of the dynamics. In Fig. 2 the temporal evolution of the phase at an exemplary point, marked by a cross in the phase plots in Fig. 1, columns I and II, is depicted in a frame rotating uniformly with the dominant frequency of the point in question, $\nu \approx 27$ mHz; see SM [26] for details. Starting with the higher illumination [Fig. 2(a)] we observe only a simple modulation with the same dominant frequency as the one of the rotating frame. This is in fact the second harmonic of the dominant frequency of the original time series $\phi(t)$ and thus stems from its slight relaxational character. In the case with the lower illumination [Fig. 2(b)], when the amplitude clusters have formed, we observe a further slow modulation of the phase evolution. This suggests that the system not only underwent a pitchfork bifurcation leading to amplitude clusters but also a secondary Hopf bifurcation creating the modulated oscillations.

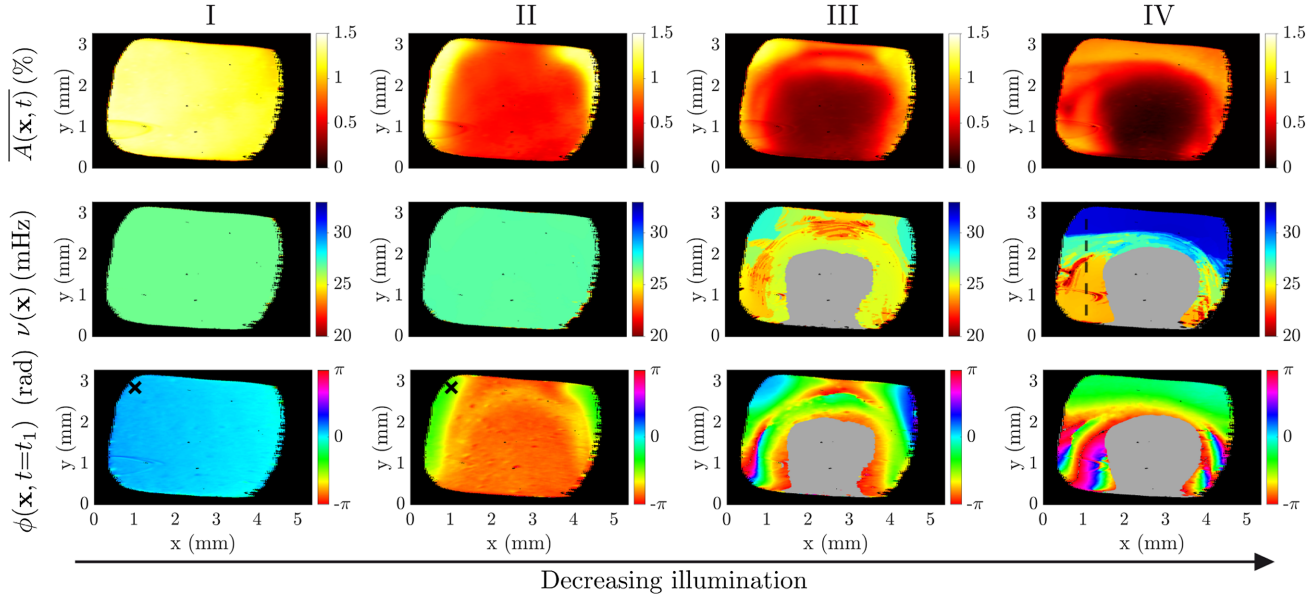

FIG. 1. Experimentally measured spatial distribution of the temporal average of the amplitude, $\overline{A(\mathbf{x},t)}$, of the dominant frequency $\nu(\mathbf{x})$, and of the phase $\phi(\mathbf{x}, t = t_1)$ at $t_1 = 807$ s at four different illumination intensities: I, $\mu = 5.97$ mW/cm^2; II, $\mu = 0.95$ mW/cm^2; III, $\mu = 0.80$ mW/cm^2; and IV, $\mu = 0.73$ mW/cm^2. Electrode size, $A = 12.19$ mm^2. The grayed out regions in columns III and IV indicate where $\overline{A(\mathbf{x},t)} < 0.35\%$ and, thus, the frequency as well as the phase cannot be determined. $\overline{A(\mathbf{x},t)}$ is given in percent of the saturation threshold of the CCD camera. Videos of the measured intensity $\xi(\mathbf{x},t)$ can be found in the SM [26].

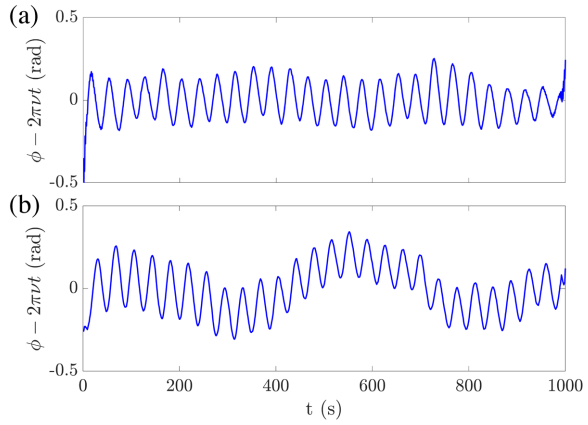

FIG. 2. Time series of the local phase in a frame rotating with the dominant frequency ν. Time series taken at the point marked by a cross in the ϕ plate in Fig. 1, columns I and II, respectively.

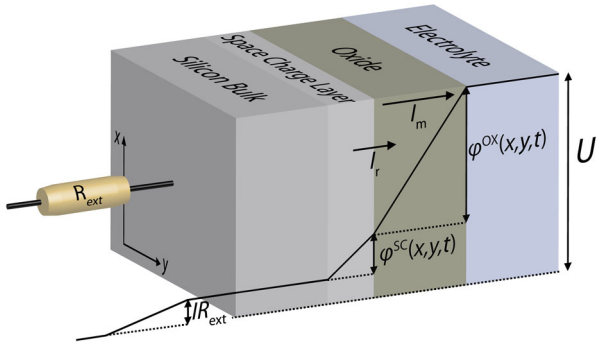

FIG. 3. Sketch of the different layers of the electrode-electrolyte interface (not to scale) and the potential drops across the different interfacial layers as well as across the external resistor. I_r, reaction current; I_m, migration current of ionic species through the oxide layer. Same x and y as in Fig. 1. For the other symbols, see text.

When lowering the illumination further, two drastic changes are observed (Fig. 1, column III). First, the mean amplitude differentiates further in space, suppressing the oscillations nearly completely on a part of the electrode. In this region, the very small amplitude combined with experimental noise leads to apparent discontinuities in the phase, rendering the determination of the dominant frequency impossible. Therefore, in the second and the third row of Fig. 1, we depict points with $\overline{A(\mathbf{x},t)} < 0.35\%$, in gray. Second, and perhaps even more astonishing, focusing our attention on the region that exhibits well defined oscillations, $\overline{A(\mathbf{x},t)} > 0.35\%$, we observe that the dominant frequency is not uniform anymore. Rather, the frequencies appear to accumulate around three plateau values, as apparent from the turquoise, red, and yellow patches in Fig. 1, column III, whereby the higher frequencies are found in the regions with higher mean amplitude.

In the last state (Fig. 1, column IV) the features that appeared in column III become more pronounced; on a part of the electrode the amplitude is practically completely suppressed. In other words, on this part of the electrode we observe amplitude death [30]. Likewise, the frequency differences across the oscillating part of the electrode become more pronounced. Equal, or at least very similar frequencies now appear in connected regions, whereby the frequency distributions of the two outer orange and blue regions are very narrow, and the frequency distribution of the middle, "mediating region" is somewhat broader, ranging from light blue to yellow. Indeed, we witness the self-organized formation of multifrequency clusters in a homogeneous oscillatory medium. Considering the snapshot of the phase distribution, we observe that the faster region at the top oscillates nearly uniformly whereas the more slowly oscillating region at the bottom exhibits a continuous distribution of the phases over 2π rad. This traveling-wave-type feature can be seen as the continuum version of a splay state in networks of coupled oscillators. Interestingly, the existence of mixed-type multifrequency clusters consisting of a splay-type cluster and a phase-synchronized cluster, as we observe it here, has also been found in simulations of networks of phase oscillators with adaptive coupling [16–18].

A key to understanding the changes in the dynamics in our system is to realize that our bifurcation parameter controls the effective number of degrees of freedom in the system. First, consider the sketch of the working electrode and the different potential drops across the cell, depicted in Fig. 3. The silicon-electrolyte interface is composed of the bulk silicon, the silicon space charge layer, the oxide layer, and the double layer (not shown). The constant applied voltage U splits into the potential drops across the external resistor IR_{ext}, the space charge layer $\varphi^{\text{SC}}(\mathbf{x},t)$, and the oxide $\varphi^{\text{OX}}(\mathbf{x},t)$ while, to a first approximation, the drops on the electrolyte side and across the bulk silicon can be neglected. At high illumination intensities, there is an excess of valence-band holes and the reaction resistance across the Si-SiO_X interface, which is, to a large part, determined by the concentration of holes n_h, is small. In comparison the resistance across the oxide and the external resistor are large and hence they limit the total current I. In this situation we observe uniform base oscillations. Moreover, any oscillations in the current lead to an oscillating potential drop across the external resistor IR_{ext} and the oxide φ^{OX} while, owing to the nearly constant concentration of holes, the potential drop across the space charge layer φ^{SC} remains constant.

As the illumination intensity is reduced, there is no longer an excess of holes since now the hole production rate and the reaction rate become of the same order, and thus the reaction resistance becomes larger. As a consequence, φ^{SC} increases at the expense of the other potential drops and the oscillations in I now lead also to oscillations in φ^{SC} and n_h.

Spatial fluctuations in $\varphi^{\mathrm{SC}}(\mathbf{x},t)$ and $n_h(\mathbf{x},t)$ lead to changes in the local current density. Moreover, they induce lateral motion of holes which is determined by the gradient of the electrochemical potential of n_h, i.e., the combination of the differences in concentration and in the electrical field (see SM [26]).

This lateral motion induces a spatial nonlocal coupling through the valence band holes. The nonlocality arises from the electrostatic potential in the space charge layer which is determined by Poisson's equation: It entails an instantaneous redistribution of the electrostatic potential in the entire layer upon any local change in the charge density. In addition to being nonlocal the coupling is also nonlinear. First, the term describing the lateral motion of the holes depends on the product of n_h and derivatives of φ^{SC} [see Eq. (5) in SM [26]]. Second, and more importantly, a change in the global current I affects the potential drop across the external resistor which in turn alters $\phi^{\mathrm{SC}}(\mathbf{x})$ and thus also n_h. Likewise, a change in n_h affects the local reaction rate ultimately feeding back into the global current.

To sum up, we have a base oscillator at high illumination that creates a global field, the total current I. At lower illumination intensity the concentration of holes becomes an additional degree of freedom which induces a spatial nonlocal coupling and feeds back to the mean field I in a nonlinear manner. Thus the dynamics can be formally described by the following equations:

$$\dot{\xi}(\mathbf{x},t) = F[\xi(\mathbf{x},t), n_h, I; \mu], \tag{4}$$

$$\dot{n}_h = G(n_h, \varphi^{\mathrm{SC}}, I; \mu). \tag{5}$$

At high illumination intensity μ, n_h remains constant and the function F in Eq. (4) represents the dynamics of the base oscillator. Equation (5) becomes relevant at low illumination intensity and depends on the mean field I that is created by the base oscillator.

If we consider our spatially continuous system as being composed of infinitesimally small base oscillators $\mathbf{w}_k$, one realizes that the nonlinear coupling is of the same type as the general physical setting for nonlinearly coupled oscillators formulated by Rosenblum and Pikovsky [5] [compare Eqs. (4) and (5) to Eq. (18) in [5]].

While in Ref. [5] the nonlinear coupling constituted a strictly global coupling, later a nonlinear and nonlocal coupling was considered [14]. Interestingly, the nonlinear nonlocal coupling supported states with three synchronized regions, each oscillating with a different frequency. In this respect, these states have a high similarity to our multifrequency clusters. However, in addition to these synchronized "frequency clustered" regions the system also contained a large incoherent domain rendering the states chimera states. In fact, looking at our data in a different way, one could argue that also our data contain characteristics of chimera states.

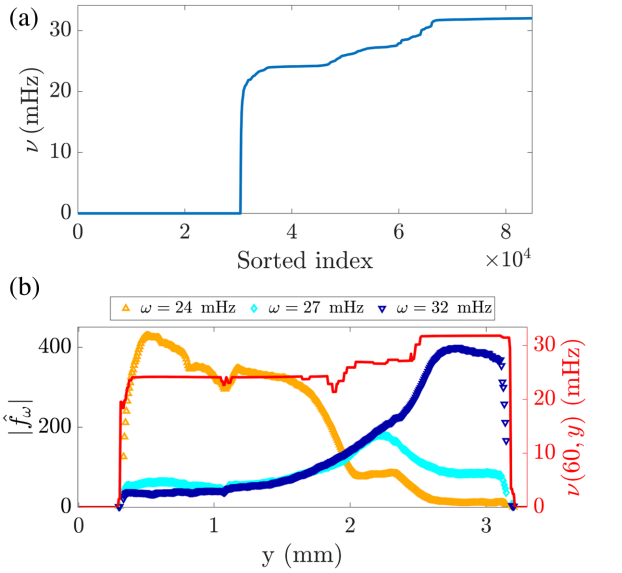

FIG. 4. (a) The dominant frequencies ν from Fig. 1, column IV sorted in ascending order. (b) Spatial profile of the absolute value of the Fourier transform of ξ for three different frequencies in mHz together with dominant frequency ν (red). Profile taken at the dashed line in the ν plate in Fig. 1, column IV.

Figure 4(a) presents a purely global picture of the dominant frequencies, neglecting any spatial information. Here, the dominant frequencies as found in state IV of Fig. 1 are sorted in ascending order. The first about thirty thousand entries with the value 0 Hz arise from the region where we observe amplitude death. For higher indices, we clearly observe three plateaus. These reflect our three frequency domains. However, the transitions between these plateaus are not sharp but instead occur continuously in a finite index range. As such, this graph is reminiscent of the distribution of dominant frequencies in the above mentioned chimera states (cf. Fig. 4 in [14]) and to some extent also to the 2-frequency chimera states in [31–33].

Also another study reveals a link between multifrequency clusters and chimera states [34]. In this study a birhythmic model was considered. When coupling these oscillators nonlocally, synchronized domains oscillating in either of the two bistable limit cycles could be stabilized.

The interfacial regions mediating between the domains with different frequencies oscillated asynchronously with frequency components of both adjacent regions. Provata interpreted her two frequency domains separated by a "more frequency" incoherent region as a chimera state. Our multifrequency cluster (Fig. 1, column IV) exhibits similar features. This can be seen in Fig. 4(b) where we present the absolute value of the Fourier coefficients of the three main frequencies, 24, 27, and 32 mHz, of the local Fourier spectra along the dashed line in the ν plot in Fig. 1, column IV. While in the bottom low- and the top

high-frequency regions the contribution of the other two frequencies are very small, in the middle region we find not only the third, dominant frequency at 27 mHz, but also a significant contribution of the frequencies of the two adjacent regions, similar to the findings in Provata's model system. Yet, since the main characteristics of our data is the coexisting of regions oscillating with different dominant frequencies, we classify the state as a multifrequency cluster noting that there is much room for further discussion about the relation between multifrequency clusters and chimera states.

Last, let us compare our findings to the multifrequency clusters in [17,18]. The decisive element in their model equations is that the coupling is adaptive, i.e., the coupling constant has its own temporal dynamics leading to different intercoupling strengths between the clusters. In our case, the hole concentration n_h is the nonlinear coupling variable, modifying the dynamics locally. From this point of view, it can be seen as establishing an adaptive coupling.

In conclusion, our experimental observation of multifrequency clusters is an exceptional example where a self-organized adaptive coupling was observed in a nonliving system, opening the door for unprecedented explorations of adaptively coupled systems in experiments.

The authors would like to thank Sindre W. Haugland, Felix P. Kemeth, Seungjae Lee, Munir M. Salman, Anton Tosolini, and Juliane Wiehl for fruitful discussions. This work has been supported by the Deutsche Forschungsgemeinschaft project KR1189/18 "Chimera States and Beyond."

*maximilian.patzauer@tum.de
†krischer@tum.de

[1] D. Golomb, D. Hansel, and G. Mato, in *Handbook of Biological Physics*, edited by F. Moss and S. Gielen (Elsevier, New York, 2001), Vol. 4, pp. 887–968, https://doi.org/10.1016/S1383-8121(01)80024-5.

[2] M. Anvari, F. Hellmann, and X. Zhang, Introduction to Focus Issue: Dynamics of modern power grids, Chaos **30**, 063140 (2020).

[3] K. Lüdge and H. G. Schuster, in *Nonlinear Laser Dynamics: From Quantum Dots to Cryptography*, edited by K. Lüdge (Wiley-VCH Verlag GmbH & Co. KGaA, Weinheim, Germany, 2011), http://doi.wiley.com/10.1002/9783527639823.

[4] K. Wiesenfeld, P. Colet, and S. H. Strogatz, Frequency locking in Josephson arrays: Connection with the Kuramoto model, Phys. Rev. E **57**, 1563 (1998).

[5] M. Rosenblum and A. Pikovsky, Self-Organized Quasiperiodicity in Oscillator Ensembles with Global Nonlinear Coupling, Phys. Rev. Lett. **98**, 064101 (2007).

[6] I. Miethe, V. García-Morales, and K. Krischer, Irregular Subharmonic Cluster Patterns in an Autonomous Photoelectrochemical Oscillator, Phys. Rev. Lett. **102**, 194101 (2009).

[7] A. A. Temirbayev, Z. Z. Zhanabaev, S. B. Tarasov, V. I. Ponomarenko, and M. Rosenblum, Experiments on oscillator ensembles with global nonlinear coupling, Phys. Rev. E **85**, 015204(R) (2012).

[8] A. A. Temirbayev, Y. D. Nalibayev, Z. Z. Zhanabaev, V. I. Ponomarenko, and M. Rosenblum, Autonomous and forced dynamics of oscillator ensembles with global nonlinear coupling: An experimental study, Phys. Rev. E **87**, 062917 (2013).

[9] K. Schönleber, C. Zensen, A. Heinrich, and K. Krischer, Pattern formation during the oscillatory photoelectrodissolution of n-type silicon: turbulence, clusters and chimeras, New J. Phys. **16**, 063024 (2014).

[10] L. Schmidt, K. Schönleber, K. Krischer, and V. García-Morales, Coexistence of synchrony and incoherence in oscillatory media under nonlinear global coupling, Chaos **24**, 013102 (2014).

[11] L. Schmidt and K. Krischer, Clustering as a Prerequisite for Chimera States in Globally Coupled Systems, Phys. Rev. Lett. **114**, 034101 (2015).

[12] L. Schmidt and K. Krischer, Chimeras in globally coupled oscillatory systems: From ensembles of oscillators to spatially continuous media, Chaos **25**, 064401 (2015).

[13] M. Komarov and A. Pikovsky, Finite-size-induced transitions to synchrony in oscillator ensembles with nonlinear global coupling, Phys. Rev. E **92**, 020901(R) (2015).

[14] M. Bolotov, L. Smirnov, G. Osipov, and A. Pikovsky, Simple and complex chimera states in a nonlinearly coupled oscillatory medium, Chaos **28**, 045101 (2018).

[15] Q. Ren and J. Zhao, Adaptive coupling and enhanced synchronization in coupled phase oscillators, Phys. Rev. E **76**, 016207 (2007).

[16] D. V. Kasatkin, S. Yanchuk, E. Schöll, and V. I. Nekorkin, Self-organized emergence of multilayer structure and chimera states in dynamical networks with adaptive couplings, Phys. Rev. E **96**, 062211 (2017).

[17] R. Berner, E. Schöll, and S. Yanchuk, Multiclusters in networks of adaptively coupled phase oscillators, SIAM J. Appl. Dyn. Syst. **18**, 2227 (2019).

[18] R. Berner, J. Fialkowski, D. Kasatkin, V. Nekorkin, S. Yanchuk, and E. Schöll, Hierarchical frequency clusters in adaptive networks of phase oscillators, Chaos **29**, 103134 (2019).

[19] G. V. Osipov, A. S. Pikovsky, M. G. Rosenblum, and J. Kurths, Phase synchronization effects in a lattice of nonidentical Rössler oscillators, Phys. Rev. E **55**, 2353 (1997).

[20] G. V. Osipov and M. M. Sushchik, Synchronized clusters and multistability in arrays of oscillators with different natural frequencies, Phys. Rev. E **58**, 7198 (1998).

[21] A. S. Mikhailov, D. H. Zanette, Y. M. Zhai, I. Z. Kiss, and J. L. Hudson, Cooperative action of coherent groups in broadly heterogeneous populations of interacting chemical oscillators, Proc. Natl. Acad. Sci. U.S.A. **101**, 10890 (2004).

[22] K. O. Menzel, O. Arp, and A. Piel, Spatial Frequency Clustering in Nonlinear Dust-Density Waves, Phys. Rev. Lett. **104**, 235002 (2010).

[23] M. Patzauer, R. Hueck, A. Tosolini, K. Schönleber, and K. Krischer, Autonomous oscillations and pattern formation with zero external resistance during silicon electrodissolution, Electrochim. Acta **246**, 315 (2017).

[24] K. Krischer, in *Advances in Electrochemical Science and Engineering* (Wiley-VCH Verlag GmbH & Co. KGaA, Weinheim, FRG, 2003), Vol. 8, pp. 89–208, https://doi.org/10.1002/3527600787.ch2.

[25] X. G. Zhang, in *Electrochemistry of Silicon and its Oxide* (Kluwer Academic/Plenum Publishers, New York, 2001), p. 510, http://link.springer.com/10.1007/b100331.

[26] See Supplemental Material at http://link.aps.org/supplemental/10.1103/PhysRevLett.126.194101 for further details and videos of the dynamics, which includes Ref. [27].

[27] S. Cattarin, I. Frateur, M. Musiani, and B. Tribollet, Electrodissolution of p-Si in acidic fluoride media modeling of the steady state, J. Electrochem. Soc. **147**, 3277 (2000).

[28] A. Pikovsky, M. Rosenblum, and J. Kurths, *Synchronization: A Universal Concept in Nonlinear Sciences* (Cambridge University Press, Cambridge, England, 2001), https://doi.org/10.1017/CBO9780511755743.

[29] K. Schönleber, M. Patzauer, and K. Krischer, A comparison of modeling frameworks for the oscillatory silicon electrodissolution, Electrochim. Acta **210**, 346 (2016).

[30] A. Koseska, E. Volkov, and J. Kurths, Oscillation quenching mechanisms: Amplitude vs. oscillation death, Phys. Rep. **531**, 173 (2013).

[31] Q. Dai, D. Liu, H. Cheng, H. Li, and J. Yang, Two-frequency chimera state in a ring of nonlocally coupled Brusselators, PLoS One **12**, e0187067 (2017).

[32] M. Mikhaylenko, L. Ramlow, S. Jalan, and A. Zakharova, Weak multiplexing in neural networks: Switching between chimera and solitary states, Chaos **29**, 023122 (2019).

[33] Y. Suda and K. Okuda, Emergence of second coherent regions for breathing chimera states, Phys. Rev. E **101**, 062203 (2020).

[34] A. Provata, Chimera states formed via a two-level synchronization mechanism, J. Phys. **1**, 025006 (2020).